1

Electromagnetic Imaging of GPR Data: Theory and Experiments

Michele AMBROSANIO[1,3], Martina Teresa BEVACQUA[2,3], Tommaso ISERNIA[2,3] and Vito PASCAZIO[1,3]

[1] *Dipartimento di Ingegneria, Università degli Studi di Napoli "Parthenope", Naples, Italy*

[2] *Dipartimento di Ingegneria dell'Informazione delle Infrastrutture e dell'Energia Sostenibile, Università Mediterranea di Reggio Calabria, Italy*

[3] *Consorzio Nazionale Interuniversitario per le Telecomunicazioni (CNIT), Parma, Italy*

Ground penetrating radar (GPR) represents a powerful technology able to investigate non-accessible scenarios in a non-invasive and non-destructive way, as witnessed by the numerous and different applications, which include demining, lunar explorations, archaeology, geology and civil engineering (Persico 2014; Sehrir et al. 2017; Aboudourib et al. 2020). However, standard GPRs provide a user-dependent map of the underground and subsurface targets, known as "radargram", whose interpretation requires firm human expertise and does not allow us to infer about the nature of the targets buried below the soil, unless some a priori information is available.

In this respect, tomographic approaches can play a very relevant role (Ambrosanio et al. 2019). These techniques aim at providing images regarding the variations of dielectric permittivity and electrical conductivity profiles of the scene

For a color version of all the figures in this chapter, see www.iste.co.uk/serhir/radar.zip.

Ground Penetrating Radar,
coordinated by Mohammed SERHIR and Dominique LESSELIER.

under investigation, which are more reliable and readable than those achieved by using standard GPR data processing. Image formation requires an accurate modeling of the scattering phenomena to properly take into account the complex interactions among sources, receivers, ground and buried objects. As a result, the development of robust and reliable recovery algorithms still has some issues related to both modeling errors as well as the presence of uncertainties in the data. Indeed, the underlying inverse scattering problem (ISP) is both nonlinear and ill-posed (Bertero and Boccacci 1998; Colton and Kress 1998).

Nowadays, most of the tomographic approaches present in the literature can be classified into three main categories (Ambrosanio 2019). The first class includes qualitative methods, which aim at detecting the scatterers hosted in the imaging domain (ID) and retrieving only a limited amount of information, such as scatter location and shape. The second ones, known as approximated methods, adopt some of the approximations of the scattering phenomena, which allow us to simplify the mathematical model and to reduce the computational complexity. Lastly, the nonlinear quantitative methods aim at retrieving both electrical and morphological properties of the ID, by tackling the problem in its full nonlinearity, without involving any approximation. A further class of imaging strategies includes hybrid approaches, which are usually based on a first qualitative step that aims at providing some rough information, that is then exploited in the next quantitative steps to avoid false solutions and to allow for reliable and effective recoveries.

In this respect, this chapter aims at providing to the research community an overview of all the main aspects on tomographic approaches in the framework of the underground exploration of the soil by GPR technologies, with particular attention given to qualitative and linearized approaches. Indeed, they can be relevant in GPR prospecting due to their simplicity and reduced computational burden.

The chapter is organized as follows. In sections 1.1 and 1.2, the equations modeling scattering problem underlying tomographic approaches is reported and extended to the case of planarly layered media. Section 1.3 introduces the basics of qualitative methods, in particular the linear sampling method (LSM), the orthogonality sampling method (OSM) and the boundary retrieval through inverse source and sparsity (B-IS) for the half-space case. In section 1.4, linearized methods are discussed, while section 1.5 is focused on regularization techniques. Finally, in section 1.6 experimental imaging reconstructions are discussed and reported from (Ambrosanio 2021).

1.1. Inverse scattering problem: mathematical formulation

In ISPs, an object-of-interest (OI) is located inside an ID Ω, which is then contained in the problem domain. The problem domain is immersed in a background medium $(\varepsilon'_b, \sigma_b, \mu_0)$ whose electrical properties are known and usually assumed to be homogeneous. It is worth noting that, for the aim of this chapter, only non-magnetic targets and background will be considered. The ID is surrounded by a boundary Γ of general shape and size depending on the employed imaging setup on which the measuring probes are located. In all of the following applications, a multi-view–multistatic system will be employed, that is, an imaging system made up of more transmitters and receivers in which the samples of scattered fields are collected at receiver locations as per each transmitting antenna.

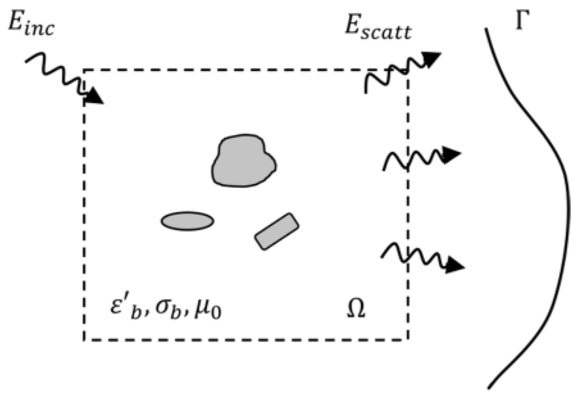

Figure 1.1. *Problem statement. The picture illustrates the incident electric field E_{inc} and the scattered electric field E_{scatt} collected at receivers locations on the curve Γ. The background is a non-magnetic medium $(\varepsilon'_b, \sigma_b, \mu_0)$ and the targets are in located the imaging domain Ω*

The whole scenario has been sketched in Figure 1.1. In general, it is possible to define the complex permittivity as:

$$\varepsilon(\vec{r}\,) = \varepsilon'(\vec{r}\,) - j\,\frac{\sigma(\vec{r}\,)}{2\pi f \varepsilon_0}, \qquad [1.1]$$

in which ε' and σ are the relative permittivity and conductivity, respectively, f is the operating frequency, $\vec{r}$ is the position vector identifying each point inside the ID, j refers to the imaginary unit and $\varepsilon_0 = 8.854 \times 10^{-12}$ F/m is the permittivity value in the void and represents a universal constant. Thus, by adopting the definition in equation [1.1], it is possible to introduce the contrast function "$\chi(\vec{r}\,)$":

$$\chi(\vec{r}\,) = \frac{\varepsilon_x(\vec{r}\,)-\varepsilon_b}{\varepsilon_b}, \qquad [1.2]$$

in which $\varepsilon_b = \varepsilon'_b - j\,\frac{\sigma_b}{2\pi f \varepsilon_0}$.

In this framework, two different electromagnetic scattering problems can be identified: the first problem, also known as *forward problem*, consists of evaluating the scattered field due to the object of interest inside the ID, assuming as known quantities both the incident field "$\vec{E}_{inc}(\vec{r}\,)$" and the contrast function "$\chi(\vec{r}\,)$" that encodes the targets properties; the second problem, also referred to as *inverse problem*, aims at estimating the unknown contrast function "$\chi(\vec{r}\,)$" from the samples of the scattered field "$\vec{E}_{sct}(\vec{r}\,)$" collected on Γ and from the illuminations "$\vec{E}_{inc}(\vec{r}\,)$". The two problems are strictly related to each other; as a matter of fact, a whole class of inversion procedure exploits the forward problem as a fundamental step for obtaining an estimate of the contrast function by means of an iterative strategy.

In order to treat these scattering problems properly, it is convenient to introduce the two equations:

$$\begin{aligned}\vec{E}^{(v)}_{tot}(\vec{r},\omega) &= \vec{E}^{(v)}_{inc}(\vec{r},\omega) + \int_\Omega \bar{\bar{G}}_i(\vec{r},\vec{r}\,',\omega)\chi(\vec{r}\,',\omega)\vec{E}^{(v)}_{tot}(\vec{r}\,',\omega)d\vec{r}\,, \\ &= \vec{E}^{(v)}_{inc}(\vec{r},\omega) + \mathcal{A}_i[\chi\vec{E}^{(v)}_{tot}]\,, \quad \vec{r}\in\Omega, \quad v = 1,\ldots,N_v,\end{aligned} \qquad [1.3]$$

$$\begin{aligned}\vec{E}^{(v)}_{scat}(\vec{r},\omega) &= \int_\Omega \bar{\bar{G}}_e(\vec{r},\vec{r}\,',\omega)\chi(\vec{r}\,',\omega)\vec{E}^{(v)}_{tot}(\vec{r}\,',\omega)d\vec{r}\,' = \\ &= \mathcal{A}_e[\chi\vec{E}^{(v)}_{tot}](\vec{r},\omega), \quad \vec{r}\in\Gamma, \quad v = 1,\ldots,N_v,\end{aligned} \qquad [1.4]$$

in which $\omega = 2\pi f$, where "(v)" represents the "V" illuminations of the multi-view–multistatic microwave system whose incident field impinges on the scatterers located in the ID, "$\vec{E}^{(v)}_{inc}$, $\vec{E}^{(v)}_{tot}$, $\vec{E}^{(v)}_{scatt}$" refer to the incident, total and scattered field at the vth illumination, respectively, while "$\bar{\bar{G}}_i$" and "$\bar{\bar{G}}_e$" are the so-called internal and external dyadic Green functions of electric type that describe the relation between the contrast function and the field generated both inside the ID Ω and the scattered field measured along the boundary Γ. These functions define the two operators introduced previously, also known as internal and external integral radiating operators "$\mathcal{A}_i$" and "$\mathcal{A}_e$" or domain and data operators, respectively. It is easy to note that such operators are bilinear related to the pair $(\chi, \vec{E}_{tot})$. These bilinear operators are defined as $\mathcal{A}_i: X \times T \to S_i$ and $\mathcal{A}_e: X \times T \to S_e$, with $X \subset L^\infty(\Omega)$ being the subspace of the possible contrast functions, $T \subset L^2(\Omega)$ being a proper subspace for the total electric field inside the object, and $S_i \subset L^2(\Omega)$ and $S_e \subset L^2(\Gamma)$ being two subspaces for the scattered field inside and outside the ID.

Rewriting equation [1.3] by exploiting the operator notation as:

$$\vec{E}_{tot}(\vec{r}, \omega) = \left(I - A_i^\chi\right)^{-1}\left[\vec{E}_{inc}(\vec{r}, \omega)\right], \qquad [1.5]$$

and substituting it in the data equation [1.4], we obtain:

$$\vec{E}_{sct}(\vec{r}, \omega) = A_e\left[\chi(\vec{r}, \omega)\left(I - A_i^\chi\right)^{-1}\left[\vec{E}_{inc}(\vec{r}, \omega)\right]\right], \qquad [1.6]$$

where "I" is the identity operator and the superscript "-1" denotes the inverse operator. Note that although the data and domain operators themselves are linear, the relation between the scattered field and the contrast function is nonlinear. The inversion of the operator in [1.6] is a mathematical representation of the nonlinearity associated with the ISP. Such an issue is handled by casting the ISP as an optimization algorithm over variables representing the unknown electromagnetic properties of the objects to be retrieved, and it occurs because of the information related to the multi-view–multistatic system.

It is worth observing that equations [1.3.] and [1.4] can be rewritten in a different form by introducing the quantity:

$$\overrightarrow{W}(\vec{r}, \omega) = \chi(\vec{r}, \omega) \cdot \vec{E}_{tot}(\vec{r}, \omega), \qquad [1.7]$$

which is known as *contrast source*. In the following, and for the scope of this chapter, the case of transverse magnetic (TM) mode will be considered. Under this assumption, the vectorial equations [1.3] and [1.4] become scalar, since only one component of the electric field is expected.

1.2. Inverse scattering problem in case of planarly-layered media

In section 1.1, a brief introduction on the mathematical statement for the ISP in a homogeneous, unbounded background medium was considered. In this section, a more suitable formulation of the concepts described in the theory of the planarly-stratified media will be dealt with.

Among all the quantities introduced previously, the main actors are still the "incident field" in the ID, the "scattered field" collected at receiver locations and the internal and external Green's functions.

For the aims proposed in this chapter, the derivation of the two-dimensional (2D) planarly-three-layered medium (known as "slab") will be considered, whose case also includes the planarly-two-layered one. These formulations belong to the framework of the simplified 2D intra-wall imaging (IWI) and GPR applications, respectively. In the following, the ID will be assumed as buried in medium 2.

To evaluate the electric field generated by a filamentary source located in a simplified 2D planarly-layered medium, the case of a single plane-wave in medium 1 impinging on the planar interface of a slab will be considered. Finally, by exploiting the Sommerfeld's (1964) identity and integrating on all the spatial frequencies, a closed-form for the incident field generated by a filamentary source in medium 1 and observed in medium 2 will be obtained.

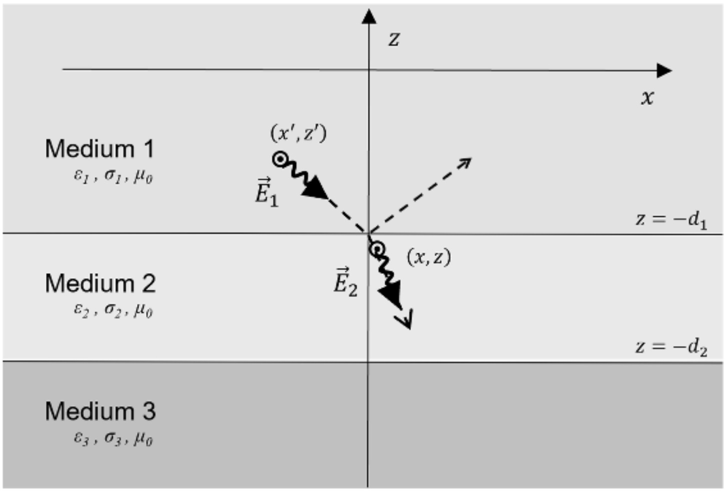

Figure 1.2. *Sketch of a planarly-three-layered medium*

For a generic 2D TM wave, the scalar electric field for a three-layered medium with source located in (x', z') and field observed in (x, z) can be written as:

$$E_{2z}(k_x, x', z, z', \omega) = A_2 e^{jk_{1z}z'} e^{jk_x x'} \left[e^{-jk_{2z}z} + R_{23}^{TM} \cdot e^{jk_{2z}(2d_2+z)} \right], \qquad [1.8]$$

in which $k_{iz} = \sqrt{\omega^2 \mu_0 \epsilon_i - k_x^2}$, with $i, j = \{1,2\}$ and $\mathcal{I}[k_{iz}] < 0$, d_2 being the depth of the related interface, and A_2 is defined as:

$$A_2 = \frac{A_1 \cdot T_{12}^{TM} \cdot e^{j(k_{1z} - k_{2z}) d_1}}{1 - R_{21}^{TM} R_{23}^{TM} e^{j k_{2z} 2(d_2 - d_1)}}, \qquad [1.9]$$

in which T_{ij}^{TM} and R_{ij}^{TM}, $i, j = \{1,2,3\}$, refers to the transmission and reflection coefficients at interface between media i and j for the TM mode, respectively, A_1 is the amplitude of the incident field and d_1 is the depth of the first interface (between mediums 1 and 2).

By choosing the reference coordinate system as making the x axis coinciding with the interface between mediums 1 and 2 (i.e. $z = -d_1 = 0$) and assuming $d = d_2 - d_1$ and unitary amplitude for the incident field in medium 1 ($A_1 = 1$), then equation [1.8] becomes:

$$\begin{aligned} E_{2z}(k_x, x', z, z', \omega) &= T_{12}^{TM} \frac{1}{1 - R_{21}^{TM} R_{23}^{TM} e^{j k_{2z} 2d}} \cdot \\ &\cdot \left[e^{j(k_{1z} z' - k_{2z} z)} + R_{23}^{TM} e^{j k_{1z} z'} e^{j k_{2z}(2d + z)} e^{j k_x x'} \right], \end{aligned} \qquad [1.10]$$

where $T_{12}^{TM} = \frac{2}{k_{2z} + k_{1z}}$ and $R_{ij}^{TM} = \frac{k_{iz} - k_{jz}}{k_{iz} + k_{jz}}$, $i, j = \{1,2,3\}$.

Finally, by exploiting the inverse Fourier transform for equation [1.10], we get:

$$\begin{aligned} E_{2z}(x, x', z, z', \omega) &= \int_{-\infty}^{+\infty} T_{12}^{TM} \frac{1}{1 - R_{21}^{TM} R_{23}^{TM} e^{j k_{2z} 2d}} \cdot \\ &\cdot \left[e^{j(k_{1z} z' - k_{2z} z)} + R_{23}^{TM} e^{j k_{1z} z'} e^{j k_{2z}(2d + z)} \right] \cdot e^{j k_x (x - x')} dk_x . \end{aligned} \qquad [1.11]$$

Thanks to the reciprocity, it is quite easy to evaluate the external Green function by replacing the observation point (x, z) with the source location and the probe location (x', z') with the receivers (Catapano et al. 2004). Finally, the internal Green's function can be written as (Chew 1995):

$$\begin{aligned} g_{int}(k_x, x', z, z', \omega) &= M_2 e^{-j k_{2z} |z - z'|} + M_2 R_{21} e^{-j k_{2z}(z + z')} + \\ &+ M_2 R_{23} e^{j k_{2z}(z + z' + 2d)} + M_2 R_{21} R_{23} e^{-j k_{2z} |z - z'|} e^{j k_{2z} 2d}, \end{aligned} \qquad [1.12]$$

which, by adding and subtracting the quantity $M_2 R_{21} R_{23} e^{jk_{2z}2d} e^{-jk_{2z}|z-z'|}$, making some calculations and exploiting the inverse Fourier Transform along the k_x direction results in:

$$g_{int}(x,x',z,z',\omega) = -\frac{j}{4} H_0^{(2)}\left(k_{2z}\sqrt{\Delta x^2 + \Delta z_-^2}\right)$$

$$-\frac{j}{2\pi}\int_{-\infty}^{+\infty} \frac{R_{23}M_2R_{21}}{k_{2z}} e^{jk_{2z}2d} \cos k_{2z}\Delta z_- e^{jk_x\Delta x} dk_x + \qquad [1.13]$$

$$-\frac{j}{4\pi}\int_{-\infty}^{+\infty} \frac{M_2}{k_{2z}} \left[R_{21}e^{-jk_{2z}(\Delta z_+)} + R_{23}e^{jk_{2z}(\Delta z_+ + jk_{2z}2d)}\right] e^{jk_x\Delta x} dk_x\,,$$

where $\Delta x = x - x'$, $\Delta z_- = z - z'$ and $\Delta z_+ = z + z'$ (Crocco and Soldovieri 2003). It is easy to derive the previous functions for the case of a two-layered medium (GPR) since it is sufficient to impose $R_{23} = 0$.

In particular, for the three-dimensional (3D) half-space case, it is possible to evaluate analytically the expression of the Green's functions by exploiting similar calculations, which drive into the formulas proposed in Lo Monte et al. (2010) and Lo Monte et al. (2012) that, for the sake of brevity, will not be dealt with in this chapter.

1.3. Solution strategies

The electromagnetic ISP defined by the previous equations is intrinsically nonlinear in the relationship between data and unknowns. However, features that are quite attractive for any inversion approach are the requirement of being fast, computationally effective and reliable from the point of view of reconstructions, trying to exploit as little a priori information as possible. Moreover, such approaches should also avoid the occurrence of false solutions, also known as "local minima" (Isernia et al. 2001).

Nowadays, all the approaches present in the literature for the solution of EIS problems can be classified into three main categories, which are as follows:

– *qualitative methods*, where only a limited amount of information is provided, such as scatterer location and shape;

– *linearized methods*, which include famous approximations such as *physical optics* and *Born approximation* (BA), or even high-order approximate models;

– *nonlinear optimization methods*, in which an approximate solution is obtained by means of an iterative process starting from an initial guess. This class will be not dealt with.

The following sections will be focused on the case of qualitative methods and linear approximations, considering some of the most adopted approaches in practical GPR scenarios.

1.4. Qualitative methods

To overcome the difficulties related to nonlinearity and ill-posedness of the inverse problem underlying GPR imaging as well as the limited number of measurements, many studies have been focused on the introduction of solution methods for the corresponding inverse obstacle problem, whose scope is to recover only the morphological information about the targets, namely their supports, giving up their electromagnetic properties (Cakoni and Colton 2006). Such methods are known as *qualitative* methods and are different from *quantitative* methods, which aim at retrieving both electrical and morphological properties of the region of interest (Cakoni and Colton 2006). Indeed, the latter tackle the problem in its full nonlinearity, without involving any approximation and allow to widen the class of retrievable objects considerably. Unfortunately, they are characterized by a higher computational burden and long processing time. On the other hand, qualitative methods are characterized by simplified mathematical models and lower computational burden. Part of the discussion about qualitative methods reported below can be found detailed in the recent paper from the same authors of the chapter (Bevacqua 2019).

Among qualitative methods, it is worth mentioning sampling methods that include the LSM (Colton 2003) (and the related factorization method; Kirsch 2008) as well as the OSM (Potthast 2010). The main idea is that of sampling the investigation domain in an arbitrary grid of points and computing in each point an indicator function whose energy will assume different values depending on whether the sampled point belongs or not to the scatter (see, for instance, Figure 1.3). Although both LSM and OSM belong to the class of sampling methods, they exhibit different features. For instance, the LSM indicator function is computed by solving an auxiliary linear problem, whose solution involves the adoption of a regularization technique. In a different fashion, the OSM does not require the solution of a linear problem, as the indicator function is just related to the evaluation of a scalar product. Moreover, the OSM seems to be more flexible with respect to the measurement configurations.

By taking advantage from recent results in area of compressive sensing and sparsity promoting techniques (Donoho 2006), a new qualitative method has been very recently introduced in literature which, provided some conditions hold true, is able to retrieve the boundary of unknown targets rather than their support (Bevacqua 2017, 2018). Such a method exploits the equivalence theorem in case of dielectric obstacles and takes advantage from the particular distribution assumed by the induced currents in case of perfect electric conductors (Bevacqua 2017). Differently from sampling methods, it does not sample the investigation domain in a grid of points, and it does not require the selection of a fixed threshold to discriminate between points inside and outside the targets. It just retrieves the boundary of the targets (see, for instance, Figure 1.3). However, if compared with LSM and OSM, it shows a heavier computational burden.

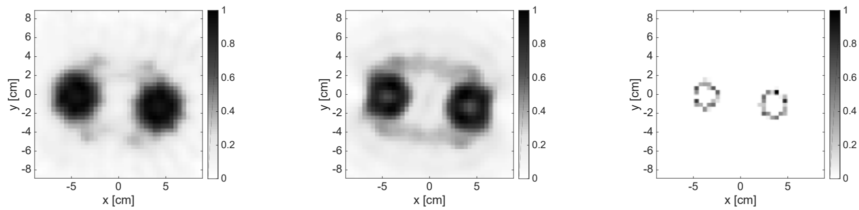

Figure 1.3. *Normalized indicators against experimental data: the TwinDielTM target. 8GHz and number of measurements M = 36. (a) LSM, (b) OSM and (c) B-IS. Extracted from Bevacqua (2019)*

1.4.1. *Linear Sampling Method*

The LSM is one of the most popular qualitative methods to retrieve objects' support from the measurements of the corresponding scattered field data (Colton 2003). In detail, it consists of sampling the region under test into an arbitrary grid of points and solving for each point the so-called *far-field integral* equation (FFE) given by:

$$\int_{\Gamma} E_{sct}{}^{\infty}(\hat{r}_m, \hat{r}_t)\ \xi(\vec{r}_s, \hat{r}_t)\ d\hat{r}_t = G_e{}^{\infty}(\hat{r}_m, \vec{r}), \qquad [1.14]$$

wherein ξ represents the unknown function, $\vec{r}_s$ is the sampling point and $E_{sct}{}^{\infty}$ is the scattered far-field pattern measured on a closed circle curve Γ in the far zone of the scatterers in direction $\hat{r}_m$ when a unit amplitude plane wave impinges from direction

$\hat{r}_t$. ${G_e}^{\infty}$ is the Green's function in the far-field zone. Despite the linearity of [1.14], the evaluation of the solution ξ is not straightforward due to the compactness of the operator at the left-hand side, which implies ill-posedness in its inversion (Bertero 1998). Hence, a regularization technique is required. An effective choice is that of solving it by adopting the Tikhonov regularization (Catapano et al. 2007). Then, the estimation of the unknown support is pursued by evaluating the l_2 norm (i.e. the "energy") of the unknown function ξ with respect to $\hat{r}_t$ given by:

$$I_{LSM}(\vec{r}_s) = \|\xi(\vec{r}_s, \hat{r}_t)\|_2^2 = \int_{\Gamma} |\xi(\vec{r}_s, \hat{r}_t)|^2 d\hat{r}_t. \quad [1.15]$$

The above defined indicator depends on the sampling point $\vec{r}_s$ and assumes a finite value when the sampling point belongs to the unknown object, while it blows up elsewhere (Catapano et al. 2007). As such, by selecting a fixed threshold, the indicator [1.15] allows the discrimination between points inside and outside the scatterers and finally retrieve the support of the target (Catapano et al. 2007). It is worth underlining that the computational burden is low, as the solution of [1.14] only involves the evaluation of the SVD of the measured data. The method has been also extended to the case of subsurface imaging (Catapano et al. 2008).

Note that, in case of a lossy background, there is the need of a modified indicator due to the attenuation of the field radiated by a buried electric dipole according to a factor which depends on the amount of losses in the host medium. Then, the energy of the LSM solution is normalized to the energy of the known term of the FFE. As a matter of fact, the field to be matched in the LSM equation becomes progressively less intense when the distance between the sampling point and the measurement domain grows. Interestingly, the presence of losses is not the only case, wherein the modified far-field equation can play a useful role. For example, for a given measurement domain and a given domain under test, in case the directions of the test dipole (whose polarization is chosen equal to the transmitting one) and the measurement dipoles do not match, the different amount of polarization mismatches, which is experienced for different depths implying very different energies for the right-hand term (Catapano 2008).

1.4.2. *Orthogonality sampling method*

The OSM has been recently introduced in literature in case of free space (Potthast 2010). It consists of computing the *reduced scattered field* from the far-field pattern ${E_{sct}}^{\infty}(\hat{r}_m, \hat{r}_t)$. Such a reduced field can be computed by evaluating the scalar product between the far-field and the Green's function in far-field zone, that is (Potthast 2010):

$$E_{sct}{}^{red}(\vec{r}_s, \hat{r}_t) = \int_\Gamma E_{sct}{}^{\infty}(\hat{r}_m, \hat{r}_t)\, e^{jk_b\, \vec{r}_s \cdot \hat{r}_m}\, d\hat{r}_m = \frac{1}{\gamma} \langle E_s{}^{\infty}, G_e{}^{\infty} \rangle_\Gamma \qquad [1.16]$$

where $\langle \cdot,\cdot \rangle$ denotes the scalar product and γ is a constant for a fixed frequency (Bevacqua 2020). In a nutshell, equation [1.16] tests the *orthogonality* relation between the far-field pattern and the Green function in far zone (apart from a constant). Then, the OSM indicator $I_{OSM}(\vec{r}_s)$ is defined as:

$$I_{OSM}(\vec{r}_s) = \left\| E_{sct}{}^{red}(\vec{r}_s, \hat{r}_t) \right\|_2^2 = \int_\Gamma \left| E_{sct}{}^{red}(\vec{r}_s, \hat{r}_t) \right|^2 d\,\hat{r}_t \qquad [1.17]$$

and achieves large values when the far-field pattern approaches the one of the background Green's function for the considered sampling point (Bevacqua 2020). Again, by selecting a fixed threshold, it is possible to discriminate sampling points belonging to the support (Bevacqua 2020).

The method has been also extended to the case of near-field (Akinci 2018b) subsurface imaging (Akinci 2018a). However, further investigations are required to better understand its physical interpretation in case of a non-homogeneous scenario.

1.4.3. *Shape reconstruction via joint sparsity based inverse source and equivalence principles*

To deal with inverse obstacle problems, we can also take advantage from the joint solution of a number of related *inverse source* problems, which consist of recovering the induced currents from the knowledge of the measured far-field pattern. The strategy is obviously suggested by the fact that the support of the contrast sources W induced in the unknown object is exactly equal to support of the target whatever E_{inc}. Note that inverse source problems are linear (see equation [1.4]) but are still (severely) ill-posed, so that some additional care is needed.

In this respect, note that when a generic electromagnetic field is propagating in the space in presence of dielectric obstacles, it induces inside the obstacles some currents, which are expected to be different from zero inside the target support and become in turn sources of the scattered field data. However, by virtue of the equivalence theorem (Franceschetti 2013) (which is a key point of the approach), the measured scattered field can be eventually conceived as the one radiated by some equivalent surface currents, that is, electric W_s and magnetic W_{smx} and W_{smy} surface currents, which can play the role of the original ones.

The main advantage of considering the equivalent currents rather than the original ones is that they are distributed over the boundary of target support. As a result, they can be identified by only few non-zero pixels in the investigation domain and, hence, can be considered sparse with respect to the pixel basis representation. Then, a possible idea for their retrieval is that of looking for the sparsest currents distributions that contemporarily satisfy the measured data. To this end, sparsity promoting approaches can be exploited (Donoho 2006).

Interestingly, the property of sparsity displayed by the equivalent currents holds true, regardless of the direction of illumination $\hat{r}_t$ or the kind of measurements configuration. To enforce this joint sparsity among the different scattering experiments, an auxiliary variable I_{BIS} can be defined as the common upper bound on the amplitude of the equivalent currents for the different scattering illumination conditions. Accordingly, the problem is recast as (Bevacqua 2017, 2018):

$$\min \| I_{BIS}(\vec{r}) \|_1 \tag{1.18a}$$

$$s.t. \quad \left\| E_s^{\infty} - \mathcal{A}_e[W_s] - \mathcal{A}_{mx}[W_{smx}] - \mathcal{A}_{my}\left[W_{smy}\right] \right\|_2 \leq \delta, \tag{1.18b}$$

$$\begin{aligned} &|W_s(\vec{r}, \hat{r}_t)| \leq I_{BIS}(\vec{r}), \\ &|W_{smx}(\vec{r}, \hat{r}_t)| \leq I_{BIS}(\vec{r}), \quad \forall\, \hat{r}_t \in \Gamma \\ &\left|W_{smy}(\vec{r}, \hat{r}_t)\right| \leq I_{BIS}(\vec{r}), \end{aligned} \tag{1.18c}$$

where $\|\cdot\|_1$ is the l_1 norm, and $\mathcal{A}_{mx}$ and $\mathcal{A}_{my}$ are the integral radiation operators which relate the magnetic surface currents to the scattered electric fields.

The variable I_{BIS} does not depend on the direction of illumination $\hat{r}_t$, but only on the position $\vec{r}$ in the investigation domain. Moreover, it is expected to assume non-zero values only on the boundary of target support, so that it will act as a "boundary" indicator. For this reason, the method is called B-IS. As such, differently from LSM and OSM, there is no need for a thresholding to retrieve the target support from the indicator map, as the approach directly retrieves the boundary of the targets.

Note that the approach can be also applied to the case of perfect electrical conductors. In fact, in such a case, the induced currents W exist only on the boundary of Σ and there is no need to introduce equivalent surface currents. Then, the problem [1.7] is further simplified (Bevacqua 2017, 2018).

The B-IS method belongs to the class of the joint sparsity promoting procedures. Note, the joint sparsity used herein is not enforced by means of the mixed norm $l_1 - l_2$ as in Kowalski (2009) and Fornasier (2008), but through the auxiliary variable I_{BIS}.

1.4.4. *Applicability and limitations of the three methods*

In LSM, the far-field equation [1.14] can be interpreted as an attempt to synthetize induced currents such that their radiating part is focused and/or circularly symmetric with respect to the given sampling point (Catapano 2007; Di Donato 2011). As such, it correctly works as long as the object is convex, and the nonradiating component of the induced currents is negligible (Catapano 2007). Usually, when the product of the maximum amplitude of the contrast χ times the maximum size of the target is large, which corresponds to an increasing amount of nonradiating sources, it does not guarantee reliable reconstructions.

The OSM is based on a test of orthogonality that allows us to compute the reduced scattered field. As far as its physical interpretation is concerned, it has been recently argued in Bevacqua (2020) that the reduced scattered field is related to the radiative part of the currents. As such, similarly to LSM, the OSM indicator does not take into account the nonradiating part of the currents, so that, again, limitations are expected with increasing electrical dimensions of the scatterer.

While both the LSM and OSM act on volumetric currents that are located on all points belonging to the support of the target, B-IS aims at jointly solving several inverse source problems, wherein one is looking for currents which (under some reasonable hypotheses) are located on the boundary of target support. Notably, the optimization problem [1.18] does not aim at retrieving exactly the equivalent currents but rather to find a common upper bound to their amplitudes. Also note the possible (superficial) nonradiating currents do not seem to play any role in the process, while the possible nonradiating volumetric currents are filtered out by the sparsity regularization. The B-IS method can be understood as more robust with respect to the presence of nonradiating currents than LSM and OSM. Moreover, the upper bound in [1.18] can be understood as a trade-off between sparsity promoting and data fitting. As a result, B-IS will be able to retrieve at least the convex-hull of the targets. Remarkably, probably because of the use of the l_1 norm rather than the l_0 pseudo-norm, we can also retrieve the shape of some non-convex target (Bevacqua 2017). As a result, B-IS is expected to fail when the boundary of the target is not sparse (for instance in case of a ragged boundary) or when, according to the sparsity theory (Donoho 2006), the number of measurements is not sufficiently large with respect to the degree of sparsity of the target contour.

Concerning the requirements about the kind of measured data, the LSM needs to correctly discretize the integral operator in [1.14] by collecting a sufficient number of data in multi-view–multistatic measurement configuration. As a result, even if the product of the maximum amplitude of the contrast χ times the maximum size of the target is not large; the undersampling of the measured data can compromise the reconstructions. On the other side, the OSM requires an accurate discretization of the integral [1.16] over the measurements curve and, hence, a sufficient number of measurements. However, differently from LSM, OSM can compensate the low amount of data by considering other kind of experiments different from multi-view–multistatic ones. In fact, OSM as well as B-IS exhibit wide flexibility with respect to processed data and can offer the possibility of combining information arising from frequency diversity without the need of a posteriori merging the single results. To this end, the OSM indicator can be easily modified by integrating over a given frequency band (Potthast 2010; Bevacqua 2020), and the B-IS indicator function implicitly defined by [1.18c] can be redefined as the upper bound to the different sources at the different frequencies (Bevacqua 2017).

Another important difference among the methods regards the computational burden. The OSM indicator does not involve the solution of an ill-posed problem but only the evaluation of a scalar product. This implies more robustness with respect to measurement errors on the scattered data and a very low computation burden. On the contrary, the LSM indicator function is computed by solving an auxiliary linear problem, whose solution involves the adoption of a regularization technique. However, the main computational effort of the method is the evaluation of the SVD of measured data, whose dimension is only dictated by the number of scattering experiments. This task must be carried out only once, since the kernel of the linear system is the same for all sampling points. With respect to the LSM and the OSM, B-IS exhibits a heavier computational burden, which drastically increases with the number of unknowns, since an l_1 norm optimization problem has to be solved. On the other side, the problem underlying the B-IS belongs to the class of convex programming problems, whose single optimal solution can be reached by any off-the-shelf local optimization procedure.

In terms of reconstruction accuracy, both the LSM and OSM require the selection of a fixed threshold to discriminate between points inside and outside the targets. In a different fashion, the B-IS does not provide an indicator map monotonically increasing outside the actual support, but directly looks for the boundary of the target. As such, it is expected to be more accurate.

1.5. Linearized methods

As a countermeasure to nonlinearity, linearized methods allow a very easy implementation and require a limited amount of computer memory and computational time, even though they suffer from several limitations induced by the adopted approximated model. These limitations can be more pronounced in the case of GPR surveys where data are collected only in reflection mode, especially in the case of single-frequency data processing.

The most popular approximation of the tomographic model [1.5] is the BA (Lo Monte et al. 2010; Ambrosanio et al. 2015). In BA, the tomographic problem is linearized as the auxiliary unknown total field inside the object is assumed equal to the known incident field. This hypothesis is satisfied in case of weak scatterers, that is, for objects whose internal characteristics are very close to the ones of the hosting medium, and/or for objects whose dimension is very small in terms of the wavelength in the hosting medium. When such assumptions do not hold true, BA can be properly exploited to perform target location. This can be also explained by considering that, in case of far-field measurements and incident plane wave, the BA operator is very closely related to the one of Kirchhoff approximation (KA) (Soldovieri 2008). The KA, or physical optics approximation, can be adopted in case of electrically large perfect electric conductors. Under such a linear approximation, the solution algorithm is formulated as the inversion of a linear integral operator that relates the scattered data to a distribution unknown function that is directly related to the illuminated boundary of the object. Therefore, the inversion allows the retrieval of target support boundary of the object.

Another relevant linearized approach has been introduced in the last few years within the virtual scattering experiments (VE) framework (Bevacqua et al. 2016). The approach is based on a proper linear combination of the original incident (in Ω) and corresponding scattered fields (on Γ) to introduce new (virtual) experiments. In this framework, a novel approximation to effectively linearize the scattering problem, even in the case of non-weak scattering regime, is introduced.

1.5.1. *Born approximation*

In the BA, the unknown total field inside the object is approximated with the incident field, that is, the object is considered negligible and therefore such a hypothesis is fully satisfied when the internal characteristics of the scatterers are close to those of the external hosting medium and its dimensions are small compared to the wavelength in the considered medium. Under these assumptions, equation [1.6] becomes:

$$E_{sct}^{(v)} = \mathcal{A}_e\left[\chi E_{inc}^{(v)}\right] = \mathscr{L}^{(v)}[\chi], \quad v = 1, \dots, N_v. \qquad [1.19]$$

The operator "$\mathcal{L}^{(v)}$", incorporating $E_{inc}^{(v)}$ in $\mathcal{A}_e$, is a linear mapping between data $E_{scat}^{(v)}$ and unknowns χ. It is worth pointing out that the linearization of model [1.6] into [1.19] does not overcome the ill-posedness of the considered inverse problem due to the finite dimensional nature of the scattered field. The order of the finite dimensional nature reduces further when accounting the aspect-limited nature of the GPR configuration. The more critical the aspect-limited is, the lower the order of the finite dimension and the more critical the capability to recover profiles. Hence, to improve the reconstruction performance of the tomographic approach, we can collect more information by using multifrequency data, since monochromatic data may be too poor to guarantee good results, as proven by the spectral coverage of the multi-view–multistatic multifrequency configuration (Leone and Soldovieri 2003; Ambrosanio and Pascazio 2015).

In choosing a multifrequency approach some attention must be paid in defining the unknown of the problem, since the contrast function does not change with the illumination, but it changes with frequency. Nevertheless, the fact that the contrast function changes with the frequency would imply solving more monochromatic ISP, but since the dependence on the frequency in the complex permittivity of the media and buried objects is supposed to be as:

$$\varepsilon(\vec{r}, \omega) = \varepsilon'(\vec{r}\,) - j\frac{\sigma(\vec{r}\,)}{\omega\varepsilon_0}, \qquad [1.20]$$

in which $\varepsilon'(\vec{r}\,)$ and $\sigma(\vec{r}\,)$ represent the permittivity and conductivity of the second medium and buried targets, with the hypothesis that they are independent from the frequency. Keeping in mind what has been said previously, it is possible to exploit the multifrequency data to improve the amount of independent information to obtain better reconstructions. By means of simple changes in the expression of the contrast function, it is possible to recover the unknown profile at a certain frequency (e.g. the maximum one) by using all of the bandwidth information. In this framework, the unknown contrast function can be written as (Bucci et al. 2001):

$$\chi(\vec{r}, \omega) = \frac{1}{2}\left(1 + \frac{\overline{\omega}}{\omega}\right)\overline{\chi}(\vec{r}\,) + \frac{1}{2}\left(1 - \frac{\overline{\omega}}{\omega}\right)\overline{\chi}^*(\vec{r}\,) = \mathscr{B}_\omega[\overline{\chi}]\,, \qquad [1.21]$$

in which $\overline{\chi}(\vec{r}\,) = \chi(\vec{r}, \overline{\omega})$ is the value of the contrast function at the selected frequency and the mathematical symbol "$*$" represents the conjugate operation and $\mathcal{B}_{\omega}[\cdot]$ represents a linear operator. Therefore, by looking at [1.21], by knowing the contrast function at the frequency $\overline{\omega}$, it is possible to evaluate the contrast function at any frequency in the selected bandwidth.

Therefore, if we consider N_f working frequencies spanning a total bandwidth $(\omega_{max} - \omega_1)$ and assume as reference the maximum frequency in the selected bandwidth, which means to assume that $\chi(\omega_{\max}) = \chi(\overline{\omega}) = \overline{\chi}$, then starting from equation [1.19] for the single-frequency case and moving toward a multifrequency approach, it is possible to write the system of equations in a compact form for the multifrequency case:

$$E_{sct}^{MF}(\vec{r}\,) = \mathcal{A}_e^{MF}[\mathcal{B}_{\omega}[\overline{\chi}(\vec{r}\,)] \cdot E_{inc}^{MF}(\vec{r}\,)] = \mathcal{L}^{MF}[\overline{\chi}]. \qquad [1.22]$$

which generalizes the BA to the multifrequency case.

1.5.2. *Distorted Born approximation*

Conversely from the linearization introduced in the previous section via the BA, such a linearization can also be performed in another scenario different from the homogeneous background, which yields the so-called distorted Born approximation (DBA). In this case, the linearization is performed about an assigned reference permittivity function (possibly inhomogeneous) and the actual internal field is approximated by the unperturbed field. This approximation is connected to the fact that in several applications, a reference dielectric permittivity, which represents a priori information about the unknown profile, can be available, so the problem can be recast as the reconstruction of the difference between the actual and the reference profiles from the scattered field data (Devaney and Oristaglio 1983; Leone et al. 1999).

Regarding the class of retrievable functions, only a limited class of permittivity profiles can be reconstructed within the DBA even if the maximum deviation from the true profile with respect to the reference profile is small. Moreover, the number and variability of these profiles can depend on the reference permittivity. However, the DBA allows the increase in the class of retrievable profile with respect to the case of simple BA.

Thus, with respect to the linear model shown in equation [1.19], the main difference consists of updating the Green's function for the specific inhomogeneous reference medium and the possible boundary conditions, and consequently also the related incident field. Unfortunately, such a function is usually not available in closed form except for special canonical geometries: in all the other cases, numerical evaluation can be exploited to obtain an estimate.

Therefore, equation [1.19] can be rewritten (in the single-frequency case) as:

$$E_{sct}^{(v)} = A_e^{bck}\left[\chi E_{bck}^{(v)}\right] = \mathscr{L}_{bck}^{(v)}[\chi], \quad v = 1, \dots, N_v. \qquad [1.23]$$

1.5.3. *A linear approach for quantitative subsurface imaging based on VE*

In order to avoid nonlinear optimization for quantitative imaging, a linear data-driven approximation has been recently developed in Crocco et al. (2012) and successively extended to GPR prospecting in Bevacqua et al. (2016). The approach has been introduced as a new scattering approximation based on the physical meaning of LSM, but a more general understanding and interpretation can be also given with respect to the framework of VE (Di Donato et al. 2015).

The linear approximation relies on a proper linear combination of the original incident in the investigation domain and the corresponding scattered fields on the measurement domain to introduce new (virtual) experiments. In case of the subsurface survey, both the VE design equation (that is the LSM equation) and the field approximation must be readapted by considering the presence of the interface between air and soil (Bevacqua et al. 2016).

The solution of the LSM is exploited to image the support indicator and choose P evenly spaced points, known as a "pivot point" $\vec{r}_p$, to build the *multi-pivot* VE experiments (Di Donato et al. 2015). Indeed, the LSM design equation [1.14] can be understood as the attempt to recombine the original scattered field in order to fit at the measurement positions $\vec{r}_m \in \Gamma$, the field radiated in the air by an elementary source placed in the soil in the considered sampling point $\vec{r}_s$.

Then, for each VE, when the pivot point $\vec{r}_p$ is inside the scatterer's support, the virtual total field $\mathcal{E}_{tot}$ can be conveniently approximated by means of the following expression:

$$\mathscr{E}_{tot}(\vec{r}, \vec{r}_p) \approx \mathscr{E}_{inc}(\vec{r}, \vec{r}_p) + LP\left[G_i(\vec{r}, \vec{r}_p)\right], \qquad [1.24]$$

where $\mathcal{E}_{inc}$ is the virtual incident field as defined in the VE framework (Bevacqua et al. 2016). Moreover, at the right-hand side, the second addendum is a low pass version of the internal Green's function. This operation avoids field singularity in the pivot point for the scattered field. It is worth underlining that this approximation takes implicitly into account the nature of the scatterer through the weighting function used to recombine the original incident field (Bevacqua et al. 2016). Moreover, in the field approximation, the unknown $\mathcal{E}$ is approximated in each $\vec{r} \in \Omega$ by considering the field G_i radiated in the soil by an elementary source placed in the same medium.

The above linear framework has a limited range of validity, as it is based on an approximation of the internal field, as well as on the validity range of the design equation, that is the FFE (Cakoni 2006). This notwithstanding exploiting the FFE as pre-processing step ensures the possibility to cope with a class of dielectric profiles (in terms of dimension and contrast values) widely exceeding the BA, as shown in Bevacqua et al. (2016). Such a property is related to the nature of the field approximation [1.5], that is *scatterer-aware* through the recombination of the data provided by LSM coefficient.

The VE framework can be exploited not only to introduce the above linearized approach, but also, and, more interestingly for the subsurface imaging problem at hand to counteract the aspect limitation of data. Indeed, aspect limited data are not sufficient to achieve quantitative characterization of the target even when the model assumptions are fulfilled, like, for example, the use of the BA in the case of weak scatterers or even assuming the exact knowledge of the internal field (the latter being an ideal case).

In this respect, the field conditioning enforced in each VE allows us also to predict the value of the field in locations other than the measurement points, so that we can exploit a number of additional equations corresponding to "fictitious measurements" (Di Donato and Crocco 2015). Accordingly, let us consider a fictitious curve Γ^* (complementary to Γ), which surrounds the investigation domain and allows us to locate measurement points in the soil. The value of the VE measured scattered field at these fictitious locations would be given by $G_i(\vec{r}_r^{\,*}, \vec{r}_p)$, where $\vec{r}_r$ and $\vec{r}_r^{\,*}$ denote the actual and the fictitious measurement points, respectively, as fictitious measurements are placed in the lower half space. As mentioned above, the virtual data equation can be suitably rewritten as:

$$k_b^{\,2} \int_{\Omega} \tilde{G}_e(\vec{r}, \vec{r}\,')\, \chi(\vec{r}\,') \mathscr{E}_{tot}(\vec{r}\,', \vec{r}_p) d\vec{r}\,' = \begin{cases} \mathscr{E}_{sct}(\vec{r}, \vec{r}_p) \; if \;\; r = r_r \in \Gamma \\ G_i(\vec{r}, \vec{r}_p) \; if \;\; r = r_r^{\,*} \in \Gamma^* \end{cases}, \qquad [1.25]$$

wherein $\mathcal{E}_{sct}$ is the virtual scattered field. To take into account the dependence of the kernel of [1.25] from the different kinds of measurement (the actual ones on surface and the fictitious one in the underground), the Green's function is defined as:

$$\tilde{G}_e(\vec{r},\vec{r}') = \begin{cases} G_e(\vec{r},\vec{r}_p) \; if \;\; \vec{r} = \vec{r}_r \in \Gamma \\ G_i(\vec{r},\vec{r}_p) \; if \;\; \vec{r} = \vec{r}_r^{\,*} \in \Gamma^* \end{cases}, \qquad [1.26]$$

that stands for the external or the internal Green's function depending on the measurement at hand.

In Figure 1.4, a sketch of the fictitious receivers, placed over the fictitious curve denoted with Γ^*, is depicted. Details about the number of fictitious receivers and the selection of Γ^* can be found in Di Donato and Crocco (2015) and Bevacqua et al. (2016).

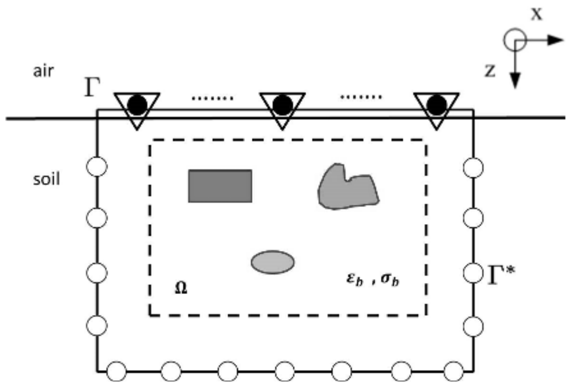

Figure 1.4. *The virtual measurements setup. The black and white circles refer to actual and fictitious measurements, respectively, while the white triangles denote the transmitters*

1.6. Regularization strategies

GPR tomography involves the solution of a severe ill-posed problem (Bertero and Boccacci 1998; Colton and Kress 1998) due to the filtering properties of the radiation operator (Bucci et al. 2001). The need for facing the low ratio between data and unknowns in the imaging problem drives the need for exploiting some regularization strategies to make the solution stable. Regularization techniques consist of adding some a priori information to the problem at hand to restore the well posedness. Such a priori information cannot be derived from the data or from the properties of the mapping which relates data and unknowns, but it is something strictly related to the expected properties of the contrast function χ to be retrieved. The effectiveness of the different regularizations will depend on how much the unknown scenario “fits” the regularization model.

The simplest form to enforce some a priori information is to include a regularizing term in the cost functional to be minimized when dealing with the inverse problem. Indeed, such an additive term will allow us to construct from the beginning a solution both compatible with the data (within the experimental error) and which exhibits the specific physical features. The additional information which can be exploited and/or enforced can be quite different. For instance, a requirement on the energy of the solution could be imposed, that is, a minimum l_2 energy requirement, which yields to the case of the well-known Tikhonov regularization technique (Colton and Kress 1998), or even some piecewise constant behavior on the contrast function (Bevacqua et al. 2016) as well as some physical bounds imposed on the permittivities and conductivities (e.g. positive permittivity and conductivities). The main issue in such a kind of regularization strategies is related to the choice of the regularization parameters, that is, the weights assigned at each regularization term, and no simple and general rules exist to perform such a choice in an optimal way.

While adding a penalty term is probably the most popular way of enforcing the regularization, there are of course other ways. Among the others, a possible strategy amounts to introduce proper statistical tools, such as in Pascazio and Ferraiuolo (2003), in which a Markov random field approach based on maximum a posteriori estimation method is proposed, which shows better performance also when compared with conventional techniques like Tikhonov regularization.

Another alternative consists of keeping the dimensionality of the unknowns space low by adopting a suitable (convenient) basis to represent the unknown function. Such a strategy is usually referred to as “regularization by projection”, as the unknown function is represented by means of a suitable set of basis functions $\{\phi_p\}_{p=1}^{P}$ as follows:

$$\chi(\cdot) = \sum_{p=1}^{P} c_p \, \phi_p(\cdot) \, , \qquad [1.27]$$

in which the c_p are coefficients of the unknown contrast and $(\cdot)$ is the independent variable (e.g. space and frequency). In a continuous space, the truncation index P should be infinite, but since we are dealing with a discrete version of the contrast function, in case of lack of any a priori information and additional forms of regularization, this number must be lower than the essential dimension of data (i.e. the degrees of freedom) and can be determined by means of an analytic or numeric criterion (Bucci and Franceschetti 1987, 1989).

As far as the choice of the basis functions is concerned, different options can be used: among them, the most adopted ones are pixel basis, spectral harmonics and Wavelet decomposition (Mallat 1999). In particular, the Wavelet basis offers the possibility to decompose the unknown profile into two sets of coefficients, namely coarse and detail coefficients, thus allowing intrinsic multiresolution representation of the unknown.

A similar idea is adopted in multiresolution regularization techniques (Bucci et al. 2001; Salucci et al. 2017). These regularization techniques allow us to accommodate the representation coefficients for the contrast unknowns in a nonuniform fashion within the investigated domain, thus allowing us to focus the processing only in those regions where the scatterers are located and to adopt a variable degree of resolution with different depths. This feature is quite interesting in GPR imaging as it permits a coarser resolution for the deeper parts of the investigated domain and preserves a higher number on unknowns for the shallower regions (Salucci et al. 2017).

In order to restore the well-posedness of the problem, another interesting opportunity is offered by the *sparsity*-based regularization techniques, which are based on the assumption that the unknown can be represented through a limited number of non-zero coefficients in a convenient basis. Such techniques guarantee that an accurate retrieval of the unknowns is possible even for a number of data much lower than the overall number of basis coefficients, but sufficiently larger than the number of non-zero elements. The most widely used sparsity based methods are probably the l_p-regularized methods, which estimate the regression coefficients by minimizing a least square objective function as (Estatico et al. 2015):

$$\Phi_p(\chi) = \|E_{sct} - \mathscr{L}[\chi]\|_{l_2}^2 + \lambda\|\chi\|_{l_p}^p , \quad [1.28]$$

where the constant $\lambda > 0$ is the regularization parameter, $\mathcal{L}$ represents the linearized GPR operator relating data (the scattered field samples E_{scat}) to the unknowns (the contrast function χ) and "p" is a parameter in the interval [0, 1].

With the advent of *compressive sensing*, a great attention has been paid to [1.28] by the signal processing community when $p = 1$. The theory of compressive sensing has shown that under sparsity and incoherence assumptions, solving the l_1-minimization problem is equivalent to solving the l_0-minimization problem (i.e.

equation [1.28]) when $p = 0$ (Figueiredo et al. 2007). In this framework, different iterative algorithms have been proposed that are based on linear programming or interior-point methods (Tan et al. 2011).

Recently, wider sparsity concepts have been explored by the research community, which are known as group-sparsity, block-sparsity or joint-sparsity. In these cases, the non-zero elements are arranged in clusters that allow us to achieve better reconstruction results than just treating the signal as being arbitrarily sparse (Sun et al. 2017; Bevacqua and Isernia 2018).

Finally, a binary regularization can be eventually considered in case of homogeneous or step wise constant unknown objects. It implies an additive term to be considered in the relevant cost functional to be minimized. The aim of this additive term is to make the punctual value of the unknown function only belong to a given finite alphabet of values $\{X_m\}$ (Catapano 2004). The values $\{X_m\}$ may be either known or unknown, depending on the available a priori information.

1.7. An example of multistatic tomographic imaging for GPR prospecting: the Gergia Tech case

In this section, BA method equipped with sparsity regularization is applied in case of an experimental multistatic GPR system developed at the Georgia Institute of Technology. The discussion and the results which follow come from the paper by Ambrosanio (2021).

The system is composed of a linear array of resistive-vee antennas (Kim and Scott 2004) made of two transmitters and four receivers arranged as in Figure 1.5. Each pair of contiguous receivers (R_1-R_2, R_2-R_3, R_3-R_4) is 12-cm spaced, while the two transmitters (T_1-T_2) are located at a 48-cm distance from each other. Thus, this arrangement of the antennas provides eight bistatic pairs spacing from 12 to 96 cm in 12 cm increments.

The GPR scanned area extends for a 1.8 × 1.8 m^2 region with the scanning system located above the surface of the ground at a constant height of 27.8 cm. The linear array of transmitters and receivers moves above the investigated area in a stepped fashion with a spatial sampling step of 2 cm. Thus, the investigated surface is discretized into a grid of 91 points by 91 points. Each time the array stops in a location, it collects data from the eight bistatic pairs by means of 401 equally spaced frequency points from 60 MHz to 8.06 GHz (i.e. a frequency step equal to 20 MHz). After collection, the data are calibrated and stored (more details regarding the data calibration are reported in Counts et al. (2007)). Note that, as far as the GPR perspective, the highest frequencies in the employed 8-GHz bandwidth are not useful due to the attenuation in the soil, while this bandwidth is efficient for the air-target test case (Ambrosanio et al. 2019).

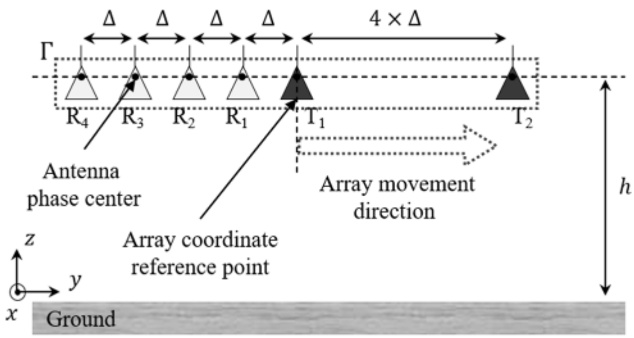

Figure 1.5. *The Georgia Tech GPR system. The spacing between contiguous receivers is Δ = 12 cm and the height from the ground is h = 27.8 cm*

The calibrated data (made available by Professor Waymond Scott[1]) require a proper pre-processing step before running the tomographic imaging procedures. The ideal clutter removal procedure consists of subtracting from the total field the one due to the clutter sources. As a matter of fact, a key factor in clutter removal techniques is the muting of the air–soil interface, as well as the estimation of its roughness (Cmielewski et al. 2007; Lo Monte et al. 2010; Temlioglu and Erer 2016; Cristofani et al. 2018).

In the following, a proper pre-processing of the data has been adopted prior to inversion. Details about the exploited strategy can be found in Ambrosanio (2021).

1.7.1. *Landmines data set*

A first experimental data set is composed of different targets that include metal spheres and a variety of anti-tank (AT) and anti-personnel (AP) dielectric mines of different sizes. Target depths range from a few centimeters up to 30 cm and the distance is to be intended from the surface of the sand to the top of the target. The ground medium is a damp, compacted sandy soil. Figure 1.6 shows a picture of the targets involved in the scenario under test and their spatial locations and depths. Both plastic AT as well as AP mines are present, together with other various objects.

1 https://waymond-scott.ece.gatech.edu/multistaticbeamformingdata/multistaticbeamformingdata/.

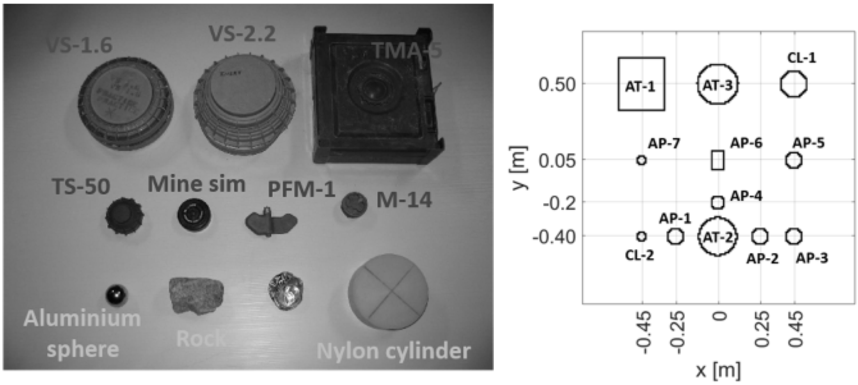

a) b)

Figure 1.6. *Targets employed for the mine data sets (a) and their spatial locations (b). The objects in red refer to anti-tank (AT) plastic mines, blue refer to anti-personnel (AP) mines and the dark yellow refer to other objects. The depths of the buried targets are as follows: AT-1 (TMA-5): 12 cm; AT-2 (VS-1.6): 11.5 cm; AT-3 (VS-2.2): 13 cm; AP-1 (TS-50): 1.5 cm; AP-2 (TS-50): 1.5 cm; AP-3 (TS-50): 2 cm; AP-4 (Mine simulant): 2 cm; AP-5 (TS-50): 1.5 cm; AP-6 (PFM1): 2 cm; AP-7 (M-14): 1.5 cm; CL-1 (Nylon cylinder): 10.5 cm; CL-2 (Aluminum sphere): 11.5 cm*

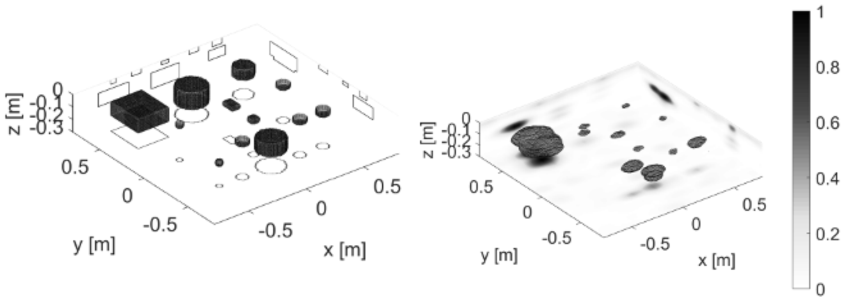

a) b)

Figure 1.7. *Reference scenario with AT and AP plastic mines and other clutter objects (a) and its recovery via multifrequency sparse BA approach (b). These results were obtained by processing 45 equally spaced frequencies in the range [0.8, 4] GHz*

To evaluate the quality of GPR recoveries, Figure 1.7(b) reports a 3D estimate of the buried targets support via exploiting sparse multifrequency BA method, while Figure 1.7(a) shows its reference. Regarding the frequency selection, 45 equally spaced frequencies in the range [0.8, 4] GHz were employed. Note that, the highest frequencies are processed as they are not useful due to the attenuation in the soil. Figure 1.7(b) shows the iso-surfaces of target supports and the colored slices representing the projections on each plane. For the sake of clarity, some slices of the retrieved profiles are reported in Figure 1.8.

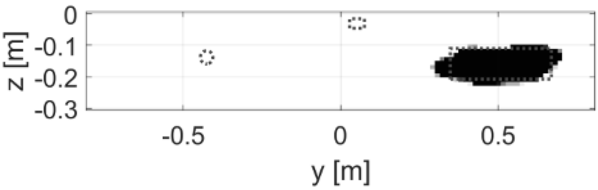

a)

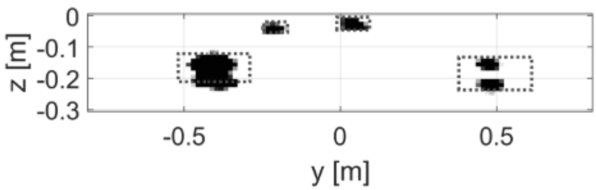

b)

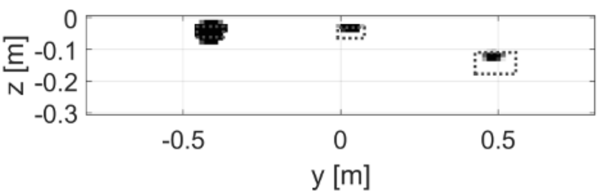

c)

Figure 1.8. *Some slices of retrieved objects supports (i.e. black areas) in Figure 1.7(b): slices at (a)* $x = -0.45$ *m; (b)* $x = 0$ *m; (c)* $x = +0.45$ *m*

Since the aim of the analysis is to provide targets support, we can assume the contrast constant with respect to the frequency, thus reducing the computational burden and memory requirement for the recovery procedure. It is worth noting that the inversion was carried out via a 2.5D procedure, that is, the GPR data corresponding to each slice are processed via a 2D algorithm despite the 3D geometry, and then each reconstructed slice along the x axis is merged with the others to cover the whole ID.

The investigated area is discretized into 33 × 108 × 24 voxels and all the slices were normalized by the largest magnitude in the whole 3D image. As expected, larger targets with higher contrasts have stronger responses: indeed, the TMA-5 AT plastic mine has a bigger retrieved support rather than other objects like the VS-1.6 and VS-2.2, notwithstanding their size. The strong contribution of the TMA-5 mine to the data might also justify the small recovery for the VS-2.2, which is worse than the one of the VS-1.6 despite their comparable size, and this might be related to its farther distance from the biggest objects in the domain. Regarding other objects like the metal sphere and the M-14 AP plastic mine, they are not visible in Figure 1.7(b) due to their small size, depth and/or composition. For similar reasons, the big nylon cylinder is not properly imaged, since its dielectric permittivity is close to that of the soil.

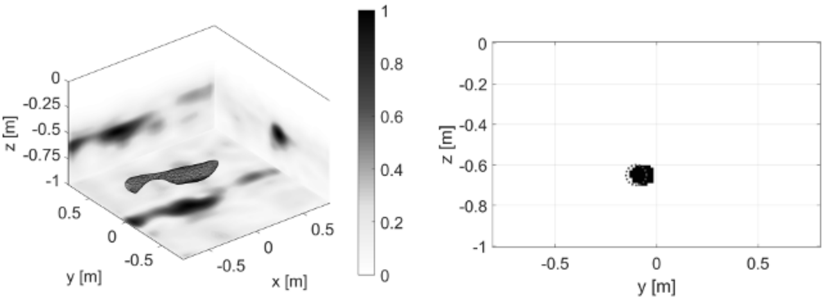

a) b)

Figure 1.9. *Support recovery of a 10 cm diameter plastic pipe buried at 58 cm (a) and its cross-section recovery at x = –50 cm. (b) A picture of the reference is reported in Counts et al. (2007)*

1.7.2. *Buried pipe*

Another example is composed of a hollow 10 cm diameter plastic pipe buried at 58 cm depth in the same sandy soil employed for the data set of landmines one.

The very accurate results of the recovery algorithm based on the use of the multifrequency BA method and iterative shrinkage thresholding algorithm (Beck and Teboulle 2009) with the same settings as described previously are reported in Figure 1.9. The threshold exploited to create the iso-surface in the image was fixed at 0.5. The figure shows clearly the location and the size of the buried pipe, as proven in (Counts et al. 2007).

1.8. References

Aboudourib, A., Serhir, M., Lesselier, D. (2020). A processing framework for tree-root reconstruction using ground-penetrating radar under heterogeneous soil conditions. *IEEE Transactions on Geoscience and Remote Sensing*, 59(1), 208–219.

Akinci, M.N. (2018a). An efficient sampling method for cross-borehole GPR imaging. *IEEE Geoscience and Remote Sensing Letters*, 15(12), 1857–1861.

Akinci, M.N. (2018b). Improving near-field orthogonality sampling method for qualitative microwave imaging. *IEEE Transactions on Antennas and Propagation*, 66(10), 5475–5484.

Ambrosanio, M. and Pascazio, V. (2015). A compressive-sensing-based approach for the detection and characterization of buried objects. *IEEE Journal of Selected Topics in Applied Earth Observations and Remote Sensing*, 8(7), 3386–3395.

Ambrosanio, M., Bevacqua, M.T., Isernia, T., Pascazio. V. (2019a). Experimental multistatic imaging via the linear sampling method. In *IEEE International Geoscience and Remote Sensing Symposium*, Yokohama.

Ambrosanio, M., Bevacqua, M.T., Isernia, T., Pascazio, V. (2019b). The tomographic approach to ground-penetrating radar for underground exploration and monitoring: A more user-friendly and unconventional method for subsurface investigation. *IEEE Signal Processing Magazine*, 36(4), 62–73.

Ambrosanio, M., Bevacqua, M.T., Isernia, T., Pascazio, V. (2021). Performance analysis of tomographic methods against experimental contactless multistatic ground penetrating radar. *IEEE Journal of Selected Topics in Applied Earth Observations and Remote Sensing*, 14, 1171–1183.

Beck, A. and Teboulle, M. (2009). A fast iterative shrinkage-thresholding algorithm for linear inverse problems. *SIAM Journal on Imaging Sciences*, 2(1), 183–202.

Bevacqua, M.T. and Isernia, T. (2017). Shape reconstruction via equivalence principles, constrained inverse source problems and sparsity promotion. *Progress in Electromagnetics Research*, 158, 37–48.

Bevacqua, M.T. and Isernia, T. (2018). Boundary indicator for aspect limited sensing of hidden dielectric objects. *IEEE Geoscience and Remote Sensing Letters*, 15(6), 838–842.

Bevacqua, M.T. and Palmeri, R. (2019). Qualitative methods for the inverse obstacle problem: A comparison on experimental data. *Journal of Imaging*, 5(4), 47.

Bevacqua, M.T., Crocco, L., Di Donato, L., Isernia, T., Palmeri, R. (2016). Exploiting sparsity and field conditioning in subsurface microwave imaging of nonweak buried targets. *Radio Science*, 51(4), 301–310.

Bevacqua, M.T., Isernia, T., Palmeri, R., Akinci, M.N., Crocco, L. (2020). Physical insight unveils new imaging capabilities of orthogonality sampling method. *IEEE Transactions on Antennas and Propagation*, 68(5), 4014–4021.

Bucci, O.M. and Franceschetti, G. (1987). On the spatial bandwidth of scattered fields. *IEEE Transactions on Antennas and Propagation*, 35(12), 1445–1455.

Bucci, O.M. and Franceschetti, G. (1989). On the degrees of freedom of scattered fields. *IEEE Transactions on Antennas and Propagation*, 37(7), 918–926.

Bucci, O.M., Crocco, L., Isernia, T., Pascazio, V. (2001). Subsurface inverse scattering problems: Quantifying, qualifying and achieving the available information. *IEEE Transactions on Geoscience and Remote Sensing*, 39(11), 2527–2538.

Cakoni, F. and Colton, D. (2006). *Qualitative Methods in Inverse Scattering Theory*. Springer-Verlag, Berlin.

Catapano, I., Crocco, L., Isernia, T. (2004). A simple two-dimensional inversion technique for imaging homogeneous targets in stratified media. *Radio Science*, 39(1), 1–14.

Catapano, I., Crocco, L., Isernia, T. (2007). On simple methods for shape reconstruction of unknown scatterers. *IEEE Transactions on Antennas and Propagation*, 55(5), 1431–1436.

Catapano, I., Crocco, L., Isernia, T. (2008). Improved sampling methods for shape reconstruction of 3-D buried targets. *IEEE Transactions on Geoscience and Remote Sensing*, 46(10), 3265–3273.

Chew, W.C. (1995). *Waves and Fields in Inhomogeneous Media*. IEEE Press, Piscataway.

Cmielewski, O., Tortel, H., Litman, A., Saillard, M. (2007). A two-step procedure for characterizing obstacles under a rough surface from bistatic measurements. *IEEE Transactions on Geoscience and Remote Sensing*, 45(9), 2850–2858.

Colton, D. and Kress, R. (1998). *Inverse Acoustic and Electromagnetic Scattering Theory*, 2nd edition. Springer, Berlin.

Colton, D., Haddar, H., Piana, M. (2003). The linear sampling method in inverse electromagnetic scattering theory. *Inverse Problems*, 19, 105–137.

Counts, T., Gurbuz, A.C., Scott, W.R., McClellan, J.H., Kim, K. (2007). Multistatic ground-penetrating radar experiments. *IEEE Transactions on Geoscience and Remote Sensing*, 45(8), 2544–2553.

Cristofani, E., Becquaert, M., Lambot, S., Vandewal, M., Stiens, J., Deligiannis, N. (2018). Random subsampling and data preconditioning for ground penetrating radars. *IEEE Access*, 6, 26866–26880.

Crocco, L. and Soldovieri, F. (2003). GPR prospecting in a layered medium via microwave tomography. *Annals of Geophysics*, 46, 559–572.

Crocco, L., Catapano, I., Di Donato, L., Isernia, T. (2012). The linear sampling method as a way for quantitative inverse scattering. *IEEE Transactions on Antennas and Propagation*, 4(60), 1844–1853.

Devaney, A.J. and Oristaglio, M.L. (1983). Inversion procedure for inverse scattering within the distorted-wave Born approximation. *Physical Review Letters*, 51(4), 237.

Di Donato, L. and Crocco, L. (2015). Model-based quantitative cross-borehole GPR imaging via virtual experiments. *IEEE Transactions on Geoscience and Remote Sensing*, 53(8), 4178–4185.

Di Donato, L., Bevacqua, M.T., Isernia, T., Catapano, I., Crocco, L. (2011). Improved quantitative microwave tomography by exploiting the physical meaning of the linear sampling method. In *Proceedings of the 5th European Conference on Antennas and Propagation*, IEEE, 11–15 April.

Di Donato, L., Bevacqua, M.T., Crocco, L., Isernia, T. (2015). Inverse scattering via virtual experiments and contrast source regularization. *IEEE Transactions on Antennas and Propagation*, 63(4), 1669–1677.

Donoho, D. (2006). Compressed sensing. *IEEE Transactions on Information Theory*, 52(4), 1289–1306.

Estatico, C., Fedeli, A., Pastorino, M., Randazzo, A. (2015). A multifrequency inexact-Newton method in L^p Banach spaces for buried objects detection. *IEEE Transactions on Antennas and Propagation*, 63(9), 4198–4204.

Figueiredo, M.A., Nowak, R.D., Wright, S.J. (2007). Gradient projection for sparse reconstruction: Application to compressed sensing and other inverse problems. *IEEE Journal of Selected Topics in Signal Processing*, 1(4), 586–597.

Fornasier, M. and Rauhut, H. (2008). Recovery algorithms for vector-valued data with joint sparsity constraints. *SIAM Journal on Numerical Analysis*, 46(2), 577–613.

Franceschetti, G. (2013). *Electromagnetics: Theory, Techniques, and Engineering Paradigms*. Springer, New York.

Isernia, T., Pascazio, V., Pierri, R. (2001). On the local minima in a tomographic imaging technique. *IEEE Transactions on Geoscience and Remote Sensing*, 39(7), 1596–1607.

Kim, K. and Scott Jr., W.R. (2004). A resistive linear antenna for ground-penetrating radars. *Proceedings of SPIE – The International Society for Optical Engineering*, 5415.

Kirsch, A. and Grinberg, N.I. (2007). *The Factorization Method for Inverse Problems*. Oxford University Press.

Kowalski, M. (2009). Sparse regression using mixed norms. *Applied and Computational Harmonic Analysis*, 27(3), 303–324.

Leone, G. and Soldovieri, F. (2003). Analysis of the distorted Born approximation for subsurface reconstruction: Truncation and uncertainties effects. *IEEE Transactions on Geoscience and Remote Sensing*, 41(1), 66–74.

Leone, G., Persico, R., Pierri, R. (1999). Inverse scattering under the distorted Born approximation for cylindrical geometries. *Journal of the Optical Society of America A*, 16(7), 1779–1787.

Lo Monte, L., Erricolo, D., Soldovieri, F., Wicks, M.C. (2010). Radio frequency tomography for tunnel detection. *IEEE Transactions on Geoscience and Remote Sensing*, 48, 1128–1137.

Lo Monte, L., Soldovieri, F., Erricolo, D., Wicks, M.C. (2012). Imaging below irregular terrain using RF tomography. *IEEE Transactions on Geoscience and Remote Sensing*, 50(9), 3364–3373.

Mallat, S. (1999). *A Wavelet Tour of Signal Processing*. Elsevier Academic Press, Florida.

Mario, B. and Patrizia, B. (1998). *Introduction to Inverse Problems in Imaging*. Institute of Physics Publishing, Bristol and Philadelphia.

Pascazio, V. and Ferraiuolo, G. (2003). Statistical regularization in linearized microwave imaging through MRF-based MAP estimation: Hyperparameter estimation and image computation. *IEEE Transactions on Image Processing*, 12(5), 572–582.

Persico, R. (2014). *Introduction to Ground Penetrating Radar: Inverse Scattering and Data Processing*. John Wiley & Sons, New York.

Potthast, R. (2010). A study on orthogonality sampling. *Inverse Problems*, 26(7), 1–8.

Salucci, M., Poli, L., Anselmi, N., Massa, A. (2017). Multifrequency particle swarm optimization for enhanced multiresolution GPR microwave imaging. *IEEE Transactions on Geoscience and Remote Sensing*, 55(3), 1305–1317.

Serhir, M. and Lesselier, D. (2017). Wideband reflector-backed folded bowtie antenna for ground penetrating radar. *IEEE Transactions on Antennas and Propagation*, 66(3), 1056–1063.

Soldovieri, F., Brancaccio, A., Prisco, G., Leone, G., Pierri, R. (2008). A Kirchhoff-based shape reconstruction algorithm for the multimonostatic configuration: The realistic case of buried pipes. *IEEE Transactions on Geoscience and Remote Sensing*, 46(10), 3031–3038.

Sommerfeld, A. (1964). *Partial Differential Equations in Physics*. Academic Press, New York.

Sun, S., Kooij, B.J., Yarovoy, A.G. (2017). Linearized 3-D electromagnetic contrast source inversion and its applications to half-space configurations. *IEEE Transactions on Geoscience and Remote Sensing*, 55(6), 3475–3487.

Tan, X., Roberts, W., Li, J., Stoica, P. (2011). Sparse learning via iterative minimization with application to MIMO radar imaging. *IEEE Transactions on Signal Processing*, 59(3), 1088–1101.

Temlioglu, E. and Erer, I. (2016). Clutter removal in ground-penetrating radar images using morphological component analysis. *IEEE Geoscience and Remote Sensing Letters*, 13(12), 1802–1806.